

Future Scenario Earthquakes Dynamic Rupture simulation on the Wenchuan-Maoxian Fault in the Longmen Shan, China, thrust belt

Tang Rongjiang¹ and Ando Ryosuke²

¹Institute of Geophysics

²University of Tokyo

November 16, 2022

Abstract

The 2008 Wenchuan Mw 7.9 mainshock has caused catastrophic destruction to cities along the northwestern margin of the Sichuan Basin. The Wenchuan-Maoxian Fault (WMF) on the hinterland side, along with a conjugate buried Lixian fault (LXF) was not activated by this earthquake but is likely to experience large earthquakes in the future. We perform 3D dynamic earthquake rupture simulations on the WMF and LXF to assess the possibility of the earthquake occurrence and further explore the possible size of earthquakes and the distribution of high seismic risk in the future. We firstly invert focal mechanism solutions to get a heterogeneous tectonic stress field as the initial stress of simulation. Then we develop a new method to refine fault geometry through inverting long-term slip rates. Several fault nucleation points, friction coefficients, and initial stress states are tested, and the general rupture patterns for these earthquake scenarios are evaluated and could fall into three groups. Depending on initial conditions, the dynamic rupture may start in the LXF, leading to magnitude-7.0 earthquakes, or start in the WMF, then cascades through the LXF, leading to magnitude-7.5 earthquakes, or both start and arrest in the WMF, leading to around magnitude-6.5 or 7.0 earthquakes. We find that the rupture starting on the reverse oblique-slip tends to jump to the strike-slip fault, but the reverse process is suppressed. The rupture propagating eastward causes larger coseismic displacements than the westward propagation, and relatively high peak ground velocities are distributed near the northeastern end of WMF.

Hosted file

supplement9.13.docx available at <https://authorea.com/users/523866/articles/595335-future-scenario-earthquakes-dynamic-rupture-simulation-on-the-wenchuan-maoxian-fault-in-the-longmen-shan-china-thrust-belt>

1 Future Scenario Earthquakes: Dynamic Rupture
2 simulation on the Wenchuan-Maoxian Fault in the
3 Longmen Shan, China, thrust belt

4 Rongjiang Tang^{1,2}, Ryosuke Ando²
5
6

7 ¹ Yangtze Delta Region Institute of University of Electronic Science and Technology of China, Huzhou,
8 Zhejiang, China

9 ² Department of Earth and Planetary Science, School of Science, University of Tokyo, Bunkyo, Tokyo,
10 Japan
11

12
13 **Corresponding Author**

14 Ryosuke Ando ando@eps.s.u-tokyo.ac.jp
15

16 **Key points:**
17
18

- 19 1. We develop a new method to refine fault geometry through inverting long-term slip rates, based on the
20 Wallace–Bott hypothesis.
21
22 2. General rupture patterns for earthquake scenarios on Wenchuan-Maoxian Fault and Lixian fault are
23 evaluated and could fall into three groups.
24
25 3. The rupture starting on the reverse oblique-slip tends to jump to the strike-slip fault, but the reverse
26 process is suppressed.

27 **Abstract:** The 2008 Wenchuan Mw 7.9 mainshock has caused catastrophic destruction to cities along the
28 northwestern margin of the Sichuan Basin. The Wenchuan-Maoxian Fault (WMF) on the hinterland side,
29 along with a conjugate buried Lixian fault (LXF) was not activated by this earthquake but is likely to
30 experience large earthquakes in the future. We perform 3D dynamic earthquake rupture simulations on
31 the WMF and LXF to assess the possibility of the earthquake occurrence and further explore the possible
32 size of earthquakes and the distribution of high seismic risk in the future. We firstly invert focal
33 mechanism solutions to get a heterogeneous tectonic stress field as the initial stress of simulation. Then
34 we develop a new method to refine fault geometry through inverting long-term slip rates. Several fault
35 nucleation points, friction coefficients, and initial stress states are tested, and the general rupture patterns
36 for these earthquake scenarios are evaluated and could fall into three groups. Depending on initial
37 conditions, the dynamic rupture may start in the LXF, leading to magnitude-7.0 earthquakes, or start in
38 the WMF, then cascades through the LXF, leading to magnitude-7.5 earthquakes, or both start and arrest
39 in the WMF, leading to around magnitude-6.5 or 7.0 earthquakes. We find that the rupture starting on the
40 reverse oblique-slip tends to jump to the strike-slip fault, but the reverse process is suppressed. The
41 rupture propagating eastward causes larger coseismic displacements than the westward propagation, and
42 relatively high peak ground velocities are distributed near the northeastern end of WMF.

43

44 **Plain Language Summary:** The 2008 Wenchuan Mw 7.9 earthquake has caused catastrophic destruction
45 to cities and counties along the northwestern margin of the Sichuan Basin. The Wenchuan-Maoxian Fault
46 (WMF) on the hinterland side, along with a conjugate buried Lixian fault (LXF) did not slip in this event
47 but is likely to experience large earthquakes in the future. We perform 3D dynamic earthquake rupture
48 simulations on the WMF and LXF to assess the possibility of the earthquake occurrence and further
49 explore the possible size of earthquakes and the distribution of high seismic risk in the future. We infer
50 the tectonic stress field from the focal mechanism solutions, to set up as the initial state of simulation.
51 Then we develop a new method to refine fault geometry through inverting long-term slip rates. We
52 simulate several earthquake scenarios, to quantify probable rupture pattern for future earthquakes in the
53 target area, the fault system of the WMF and LXF. This process is to clarify the mechanical causality of
54 the dynamic system. Numerical simulation results forecast the possible size of the earthquakes and the
55 potential high seismic risk areas occurring on the WMF and LXF in the future while the timing is out of
56 focus.

57

58 **1 Introduction**

59 The 2008 Mw7.9 Wenchuan earthquake caused devastating destruction to cities and counties along the
60 active faults of the Longmen Shan thrust belt. Three parallel NW dipping fault zones, from hinterland to
61 foreland being the Wenchuan-Maoxian fault, the Beichuan fault, and the Pengguan fault, constitute the
62 crustal structure of the Longmen Shan fault zone (LMSFZ) (Figure 1), and the mainshock and aftershocks
63 only rupture the BCF and PGF (Xu et al.,2009; Feng et al.,2017; Liu-Zeng et al., 2009). Several counties
64 including Yingxiu, Beichuan, Nanba have suffered a devastating disaster in this event, one of the obvious
65 reasons is that the fault almost passes through the center of the counties (Figure 1). Similarly, the WMF
66 also passes through the urban areas of Wenchuan, Maoxian and several towns, and more than 200

67 thousand inhabitants live in the area along this fault. Should an earthquake in the future occur on the
68 WMF, it would cause significant hazards to densely populated towns.

69 Yingxiu and Beichuan towns suffered the most intensive shock in the Wenchuan earthquake, which has
70 been confirmed by previous inversion works and dynamic models (Hao et al., 2009; Shen et al., 2009;
71 Zhang et al., 2011; Tang et al.,2021a). If numerical simulations can be used in advance to predict the
72 rupture characteristics of future earthquakes, especially the position of maximum slip patches, can the
73 huge mortality of 2008 Wenchuan earthquake be significantly reduced? If the WMF has the potential to
74 produce a strong earthquake in the future, how large the earthquakes on the WMF may occur? Dynamic
75 rupture simulations can intrinsically simulate physically self-consistent features of earthquake behavior,
76 being able to simulate an unknown earthquake given under given stress conditions and fault geometry.
77 This makes it a natural choice to investigate a future scenario earthquake on the WMF.

78 In contrast to the approach that we present in this paper, most of previous dynamic simulations have been
79 used to investigate large earthquakes that had already occurred, with abundant prior information being
80 available to constrain fault geometry and regional stress field (Zhang et al.,2019; Ando et al.,2017; Ulrich
81 et al.,2019; Tang et al.,2021a). For instance, early aftershock locations can also help constrain the
82 geometry of seismogenic fault that ruptured during the mainshock (Yin et al.,2018; Wu et al.,2017; Wang
83 et al.,2021), so do the earthquake focal mechanism solutions (FMS) containing information of
84 characteristics of the fault geometry. Many researchers use the FMSs from foreshocks or aftershocks to
85 invert the regional stress, which can be resolved onto the fault surface as initial condition of dynamic
86 earthquake simulation (Zhang et al.,2019; Ando et al.,2017; Ulrich et al.,2019). However, simulating an
87 unknown and reliable earthquake in the future, such as this work, is a challenge due to the lack of
88 sufficient seismological evidence to build a dynamic model.

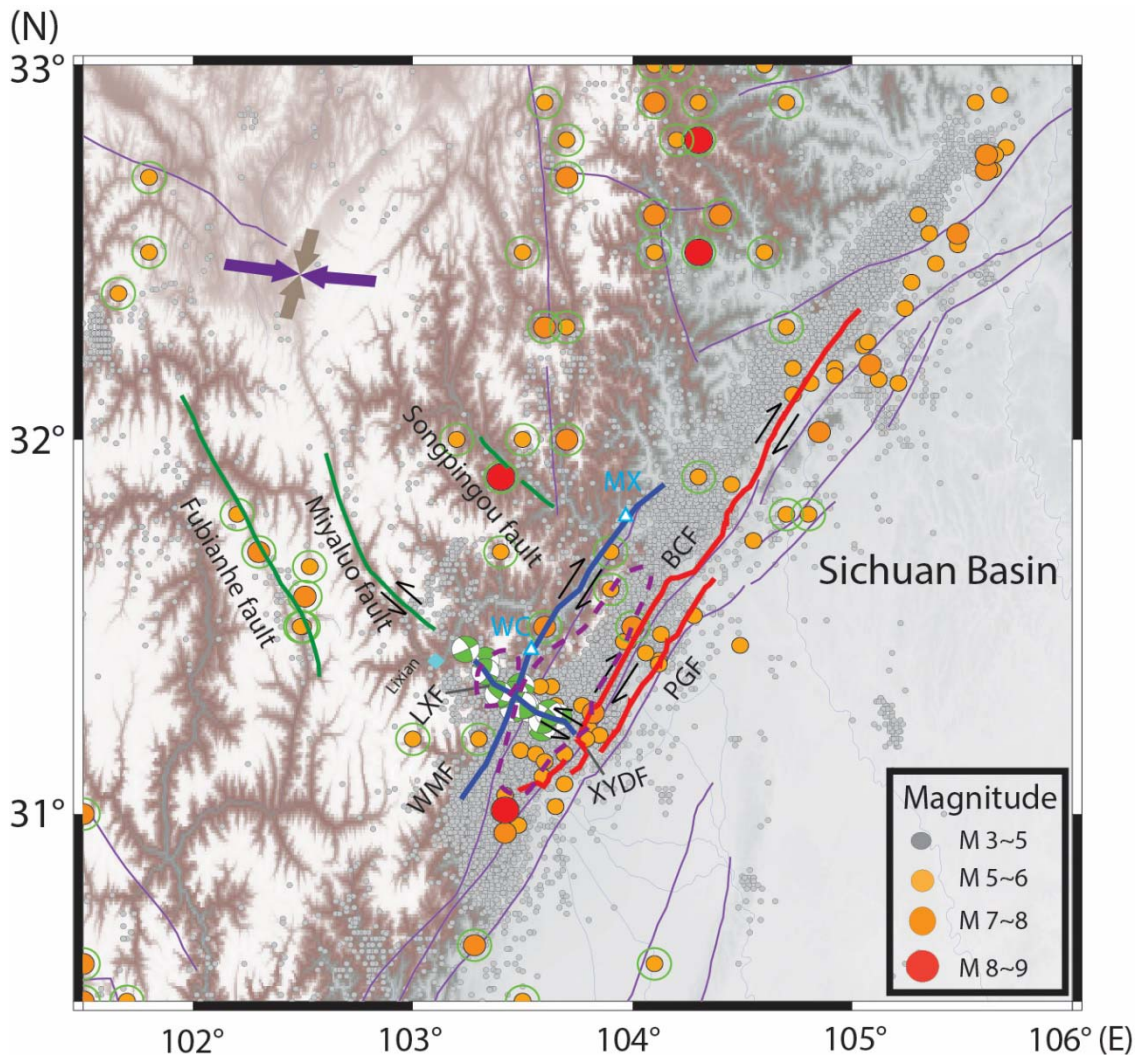
89
90 Fortunately, the WMF is close to the Wenchuan main shock: BCF, and there are still some aftershocks
91 distributed along the WMF. Together with the fact that the tectonic stress field usually changes slowly in
92 a small range, it enables us to use the focal mechanism solutions of aftershocks to invert the regional
93 stress field near the WMF. Nevertheless, the aftershocks along the WMF are very limited, especially in
94 the northern portion, which is not enough to provide accurate constrain for geometry of numerical
95 simulation (Wu et al.,2009; Zhao et al.,2010; Yin et al.,2018). To solve this problem, we propose a new
96 optimal method to obtain the fault geometry of WMF by inverting the long-term slip rate, based on the
97 Wallace-Bott hypothesis (Wallace 1951; Bott, 1959), which asserts that rigid blocks slide linearly with
98 respect to each other along a planar fault in the direction of the maximum resolved shear stress. The goal
99 of this algorithm is to find optimal geometrical parameters by the conjugate gradient method, to minimize
100 the difference of directions between long-term slip rate and tangential traction, supposing that regional
101 stress has been determined and resolved to the fault surface. In this case, we can constrain the geometry of
102 any fault using the measured long-term slip rate, regardless of whether earthquakes have been recorded
103 before.

104 It is worth pointing out that relocation of the Wenchuan earthquake sequence revealed an NW-SE-striking
105 buried Lixian fault (LXF, shown in Figure 1) with a length of ~50 km, roughly perpendicular to the WMF
106 with oblique dextral slip sense. Considerable pure strike-slip type aftershocks (Cai et al.,2011; Yi et
107 al.,2012; Li et al.,2019; Yang et al.,2021) along the LXF reveal an almost vertical fault plane and sinistral
108 strike-slip. The cross-cutting geometry and opposite slip senses of these conjugate faults raise questions

109 about fault interactions. Whether the ruptures starting from different nucleation positions cascade through
110 another fault to form a greater disaster than a single earthquake, or get arrested near the fault intersection?

111 In this study, we first calculate the distribution of heterogeneous stress fields near the WMF based on the
112 focal mechanism solutions (FMS) of earthquakes ($M \geq 3.5$). In contrast to the previous studies involving
113 tectonic stress analysis of LMSFZ (Li et al.,2019), we focus on obtaining reliable heterogeneous stress
114 tensor distribution including isotropic and deviatoric parts, such that we directly apply the inverted stress
115 to the numerical simulation, without any trial-and-error approach (Douilly et al., 2015; Ulrich et al.,2019;
116 Xu et al.,2019; Lozos and Harris, 2020) to obtain a stress condition fitted to aimed coseismic slip
117 distributions. Then, we apply the conjugate gradient algorithm to invert long-term slip rate to get the
118 optimal geometrical parameters. Subsequently, we implement the several dynamic rupture computational
119 simulations to investigate physics-based scenarios of large earthquakes on the WMF and LXF, aim at
120 exploring how big an earthquake may occur on these two faults in the future, and evaluate the possible
121 distribution of high seismic risk.

122



123

124 Figure 1 Map showing the setting of major faults of the center Longmen Shan fault zone. The red bold
125 black lines indicate the field-confirmed rupture traces in Wenchuan earthquake (Xu et al.,2009; Liu-Zeng
126 et al.,2009). The blue solid lines represent the WMF and Lixian faults, both of which did not slip in the
127 mainshock but are very active in aftershocks. The green solid lines represent three active faults parallel to
128 the LXF. Accurate fault trace of the WMF is derived from field investigation of Xie et al (2011), and the
129 location of the LXF trace is deduced from the distribution of pure strike-slip aftershocks (Li et al.,2019).
130 Historical earthquake catalog denoted by filled circles refers to Wang et al (2021) and China Earthquake
131 Networks Center (<http://data.earthquake.cn>). Green hollow circles denote the historic strong earthquakes
132 ($M > 5$) before 2008 Wenchuan event. The purple and gray coupled arrows depict the maximum, and
133 minimum horizontal compressional stress fields (Luna and Hetland, 2013). The third primary stress (not
134 shown) is vertical. The purple dashed circles respectively show the positions of Xuelongbao (north) and
135 Pengguan (south) Massif (Shen et al, 2019). WC-Wenchuan. MX-Maoxian.

136

137 **2 Seismicity and potential seismic risk in the Wenchuan-Maoxian fault and Lixian Fault**

138 Firstly, the WMF has prominent similarities in fault orientation and geometry to the BCF and PGF caused
139 the 2008 mainshock. The three faults are spatially subparallel and horizontally spaced within 20km
140 (Figure 1). Also, they may root into the same main detachment with a depth of around 20 km and the
141 main fault shapes display an essentially classic ramp-flat geometry (Hubbard et al 2010; Jia et al.,2010; Li
142 et al.,2010). The simulation of Tang et al. (2021a) reveals that Wenchuan mainshock has changed the
143 stress status on the WMF, forming a positive Coulomb failure stress change in the center portion of the
144 WMF, suggesting that the 2008 mainshock may clock-advance the earthquake cycle of the WMF, though
145 to a limited extent (the fault perpendicular extent of the stress change is limited by the seismogenic depths,
146 comparable to the fault separation of 20 km). The WMF on the hinterland side was not activated by the
147 2008 event, but we presume that this fault has potential to experience an earthquake in the future, while
148 the timing cannot be specified.

149 Second, field investigations and exhumation studies of the central Longmen Shan show that the WMF has
150 mainly exhibited dextral strike slip faulting with the comparable reverse component (Tang et al.,1991;
151 Zhou, et al.,2007; Shen et al,2019; Tian et al., 2013; Tan, Xu, et al., 2017) since the Late Cenozoic,
152 which is consistent with the coseismic slip sense as well as the long-term slip rate of BCF and PGF (Zhou
153 et al.,2007; Densmore et al., 2007; Xu et al.,2009; Liu-Zeng et al., 2009; Feng et al.,2017). Shen et al
154 (2019) collected samples from the two vertical transects from the central and southern sides of the
155 Xuelongbao massif, to extract apatite and zircon for fission track and (U-Th)/He analysis. The
156 exhumation history of the Wenchuan-Maoxian fault can be constrained to around 0.6 mm/yr of long-term
157 slip-rate, which is similar to that along the frontal BCF (~ 0.54 mm/yr before Wenchuan earthquake (Zhou
158 et al.,2007) and $0.88\sim 0.91$ mm/yr after Wenchuan event (Ran et al.,2013)), suggesting that the WMF may
159 have the comparable intensity of tectonic activity as the BCF to accommodate significant crustal
160 deformation over the long-term, even though it was not ruptured by the 2008 Wenchuan earthquake.

161 In addition, the modern earthquake catalog provides evidence that three major faults have comparable
162 seismic activities. According to observational records before Wenchuan earthquake (Figure S1), three
163 strong earthquakes ($6 < M < 6.5$) have occurred in the middle Longmen Shan: April 1657 $M 6.5$ in
164 Wenchuan, February 1950 $M 6.2$ in Beichuan and February 1970 $M 6.2$ in Dayi. A total of 11 moderate

165 earthquakes ($5 < M < 6$) in this area were distributed over three faults, with 4 earthquakes occurring near the
166 WMF, according to Data Sharing Infrastructure of National Earthquake Data Center
167 (<http://data.earthquake.cn>) (see Figure S1). Due to the low historical seismicity and limited (< 3 mm/yr)
168 geodetic observations (Chen et al., 2000), it was not until the occurrence of Ms8.0 Wenchuan earthquake
169 in 2008 that high seismic risk in the central Longmen Shan was generally realized by most researchers. It
170 is important to note, a total of 12 $M_s > 5.6$ aftershocks occurred within one year after the Wenchuan
171 earthquake, of which three occurred in the WMF and one in the LXF.

172
173 The buried Lixian fault may be active, located as bridging the WMF and the BCF, although insufficient
174 evidence has been collected on the surface. Geological survey is very scant for this fault due to the heavy
175 vegetation cover and rugged terrain, and the maximum elevation difference exceeds 3 kilometers (Tan et
176 al., 2017). Further to the northwest along the aftershock belt, the Miyaluo fault is exposed (Figure 1). It
177 displays a sinistral sense of slip with unknown slip rates and has been active during the Pleistocene (Yang
178 and Zhang, 2010; Wang et al., 2015). Yang and Zhang (2010) have dated twelve samples of
179 metasediments and granites taken from the Miyaluo Fault, WMF and BCF using apatite fission track
180 dating (FT) method. These samples were collected in the developed fracture zone of rock mass, with FT
181 ages significantly younger than the surrounding rocks, indicating the most recent tectonic activities. The
182 results show that the high activity of WMF and BCF occurred in the early Pleistocene (FT ages of $1.2 \sim$
183 1.3 Ma); the Miyaluo fault developed in the interior of the plateau was also highly active in the middle
184 Pleistocene (around 0.5 Ma). Despite the lack of direct geological evidence, we suspect that the Miyaluo
185 fault may still have been active in the Holocene, since several destructive earthquakes (larger than $M7$)
186 were recorded on the two sub-parallel faults: the Fubianhe and Songpinggou faults with NW strike
187 orientation, conjugating the BCF (Figure 1). After the Wenchuan event, it is also possible that the fracture
188 along the LXF propagates toward the Miyaluo fault in the future. In the following chapter of stress
189 inversion analysis, we will find that the LXF exhibits the most favorable orientation in the regional stress
190 field. Therefore, LXF may display a relatively high seismic risk, although none of the great earthquakes
191 has been recorded recently.

192
193 The 2008 Wenchuan main shock and aftershocks released a large amount of stress or elastic energy along
194 the BCF and PGF, resulting in a low seismic risk for a long period in the future. On the contrary, the
195 WMF has not experienced a strong earthquake for more than 360 years since the possible last $M6.5$
196 earthquake in 1657, and the current earthquake interval completely excess a moderate earthquake ($5 < M < 6$)
197 cycle (Figure S1). In addition, positive Coulomb failure stress change from 2008 mainshock may increase
198 seismic activities in the regions with loaded stress on WMF. Consequently, incorporating
199 abovementioned factors, we suggest that the WMF may have the potential to produce a strong earthquake
200 with $M > 6.5$ even $M7$ in the future, while the timing is out of focus.

201
202
203

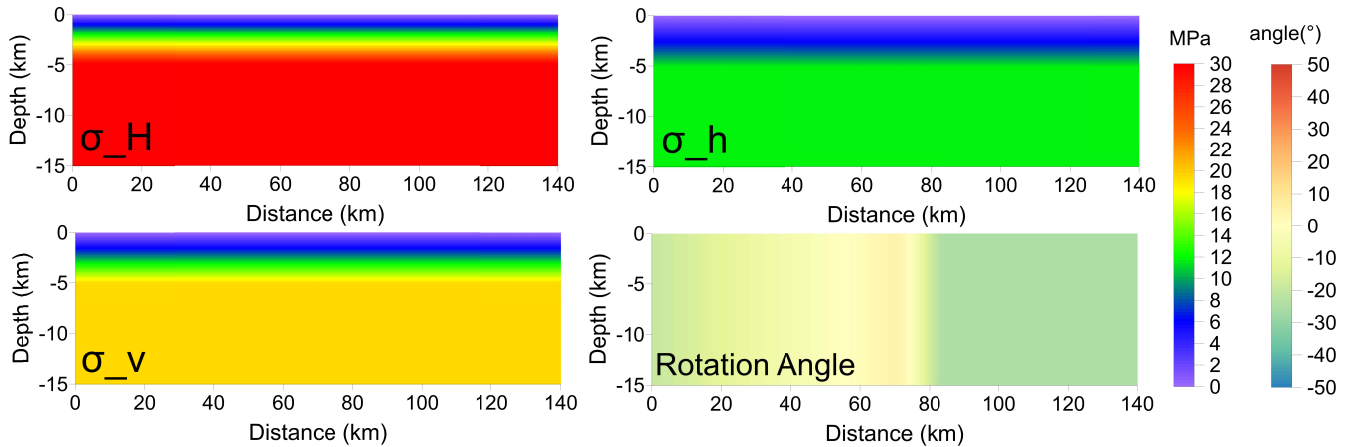
204 **3 Regional stress inversion and modeling**

205 The initial stress plays a fundamental role in controlling dynamic rupture processes. We infer the present
206 regional tectonic stress field by inverting earthquake focal mechanism solutions (from Li et al., 2019) of
207 aftershocks of 2008 Wenchuan earthquake as a reference to the future earthquake scenario in this region.
208 We adopt a damped linear stress inversion method developed by Hardebeck and Michael (2006) to

209 determine the stress field using FMSs. This method enables us to infer the directions of the principal
 210 stresses σ_r ($r = 1, 2, 3$ for the maximum, intermediate and minimum principal stresses, respectively) and a
 211 ratio between the principal stresses σ_r , defined as $\Phi = (\sigma_2 - \sigma_3)/(\sigma_1 - \sigma_2)$. The details of the method and
 212 results are described in the supplementary Text S1.

213 However, to be inputted into our dynamic rupture simulation, these observationally constrained
 214 parameters are insufficient to determine the absolute values of the principal stresses. Two unknowns are
 215 needed by imposing other prior information. For simplification, we firstly assume that one of the principal
 216 stress axes is in the vertical based on the observation near the WMF as expected from Anderson (1951).
 217 Then we constrain one unknown as the $\sigma_H/\sigma_v = 1.6$, given an approximate value from the In-situ stress
 218 measurements along the Beichuan-Yingxiu fault after the Wenchuan earthquake (Qin et al.,2013), where
 219 σ_H and σ_v denote the magnitudes of the maximum horizontal principal stress and the vertical principal
 220 stress. The σ_H along the depth is constrained by assuming the average stress drop satisfies the stress drop
 221 derived from empirical relations (Kanamori and Anderson, 1975). We assume typical overburden stress
 222 and the pore pressure increase with the depth, and the latter gradient gradually approaches the former
 223 (Rice, 1992), such that the stresses is tapered to the ambient value at a certain depth (here we set 5 km)
 224 (Rice, 1993). The resulting stress field model is shown in Figure 2 as plotted on the surface of WMF. The
 225 along-strike rotation of the principal horizontal stresses reflects our inversion result.

226
 227



228
 229 Figure 2 Along strike distribution of three-component principal stress (σ_H , σ_h for the maximum and
 230 minimum horizontal principal stresses, σ_z for vertical principal stresses). The lower right Figure shows
 231 the angle between the east and the maximum horizontal stress axis (Negative denotes the clockwise).
 232
 233

234 4 Fault Geometry modeling and new inversion method

235 Our dynamic model is built to reproduce the observed oblique dextral-slip WMF and almost pure sinistral
 236 strike-slip LXF (Figure 1). We set the LXF as vertical, with 0.5 km buried depth, as well as 15 km basal
 237 depth inferred from average seismogenic depth (Shen et al., 2009; Wan et al.,2017; Ramirez-Guzman and
 238 Hartzell, 2020). In the simulation we assume an artificial boundary on the northern end of the LXF, not to
 239 extend northward and link the Miyalu fault (Figure 1). Many studies over the last decade focused on the

240 geometry of the BCF and PGF through detailed relocation of aftershocks (Wu et al.,2009; Zhao et
241 al.,2010; Yin et al.,2018) and seismic reflection data (Hubbard et al., 2010; Jia et al., 2010; Lu et al.,2014),
242 as well as joint inversion of GPS and InSAR measurements (Shen et al.,2009; Wan et al., 2017). Yet the
243 geometry of WMF fault is still unclear so far, due to the scant investigations of seismic reflection, and its
244 aftershocks are very limited, especially in the northern portion.

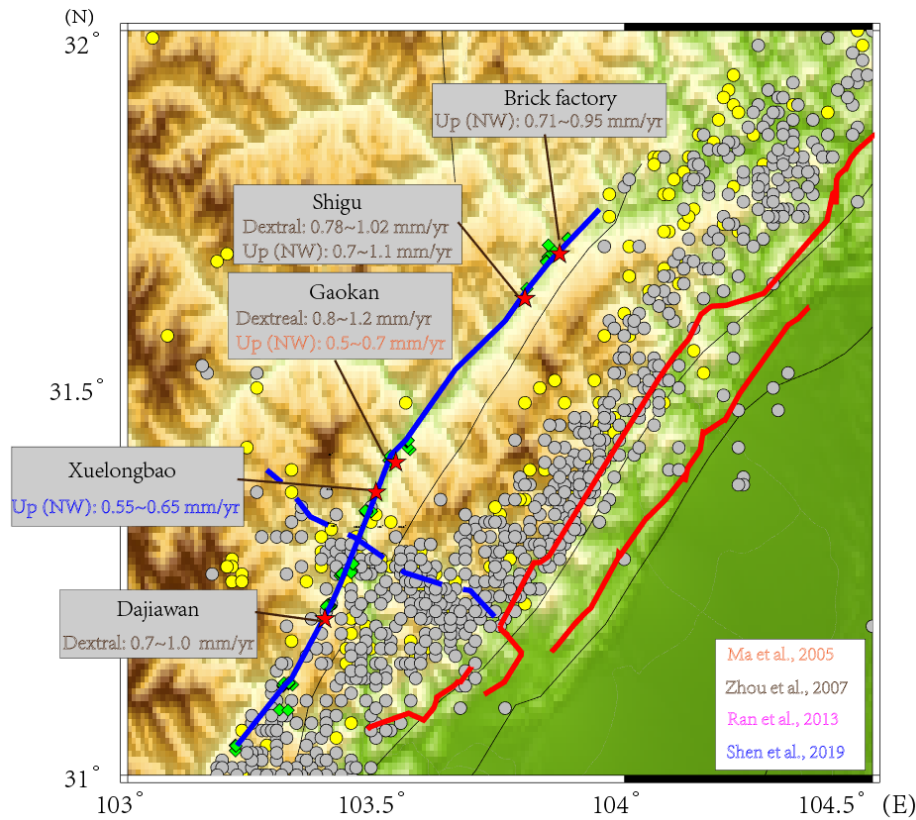
245 Here we develop a new method to refine the fault geometry of WMF by inverting the long-term slip rate,
246 based on the abovementioned regional stress field and the Wallace-Bott hypothesis (Wallace 1951; Bott,
247 1959). The basic assumption of the current method is that the slip direction (the rake angle) is parallel to
248 the maximum shear traction on the fault, determined by the inferred principal stresses and the orientation
249 of the fault plane. A model of listric fault geometry is considered, which is allowed to vary continuously
250 along strike to utilize the data of the surface fault traces. The downdip fault geometry follows the form
251 (Wan et al.,2017):

$$252 \quad z(y) = \frac{2h_0}{\pi} \arctan(y/\tau), \quad (1)$$

253 where z is the depth of the fault plane, and y is the horizontal distance of the fault plane from its surface
254 trace. The fault surface is described by the B-spline allowed to vary continuously along strike, with its
255 downdip curvature dictated by the parameter τ . h_0 is the fault depth to be solved for, and assumed to be
256 the same for all the fault segments. In this nonlinear inversion, the model parameters include a total of the
257 10 downdip curvature parameter τ uniformly distributed along the fault strike (around 16 km spatial
258 interval), plus h_0 for all curves. Under the condition that the values of τ can accurately describe the
259 surface trace and the non-planar fault surface, we expect as few parameters as possible to avoid the over-
260 fitting problem due to limited observed data. We collected both the vertical and horizontal components of
261 the long-term slip rate from a few studies (Ma et al.,2005; Zhou et al.,2007; Ran et al.,2013; Shen et al.,
262 2019) shown in Figure 3, and a total of 5 measured points with 7 slip-rates along the WMF are
263 implemented in the inversion. Although the distribution of collocation points does not well cover the
264 whole fault area, this analysis is useful to constrain the first-order feature of WMF geometry. The details
265 of our geometry inversion method are further elaborated in the supplementary Text S2.

266 Long-term slip rate can't be accurately measured due to the uncertainty of geological age estimation of
267 sediments (Zhou et al.,2007; Shen et al., 2019). To get a more reliable result, the inversion uncertainty is
268 estimated using 100 bootstrap resamplings of the entire data set (7 slip-rates), and data from each
269 measured point obey a Gaussian distribution. For each inversion, we set the same initial model with $\tau=5$,
270 $h_0 = 18 \text{ km}$ (Figure 4a). In addition, a few aftershocks are distributed at the south end of WMF (Figure
271 S2), which is useful as prior information to constrain one of the inversion parameters. We can well fit the
272 distribution of aftershocks using equation (1) with $\tau=3.5$, $h_0 = 18 \text{ km}$. Therefore, the parameter τ at the
273 southernmost position ($x = 0 \text{ km}$) is a force to keep little variation during the inversion.

274
275
276



277
278
279
280
281
282
283
284
285

Figure 3 Map showing the measured points of long-term slip rate along the WMF. Each gray box contains the locations and long-term slip rates measured from different researchers. Dextral means dextral strike-slip rates and Up (NW) vertical slip rates with northwestern block being hanging wall. The red and blue lines are the same with Figure 1. Accurate fault trace of the WMF is from field investigation (green diamonds) of Xie et al (2011), and red stars denote the measured point positions of long-term slip rate. Gray circles present aftershocks of the 2008 earthquake (Yin et al.,2018).

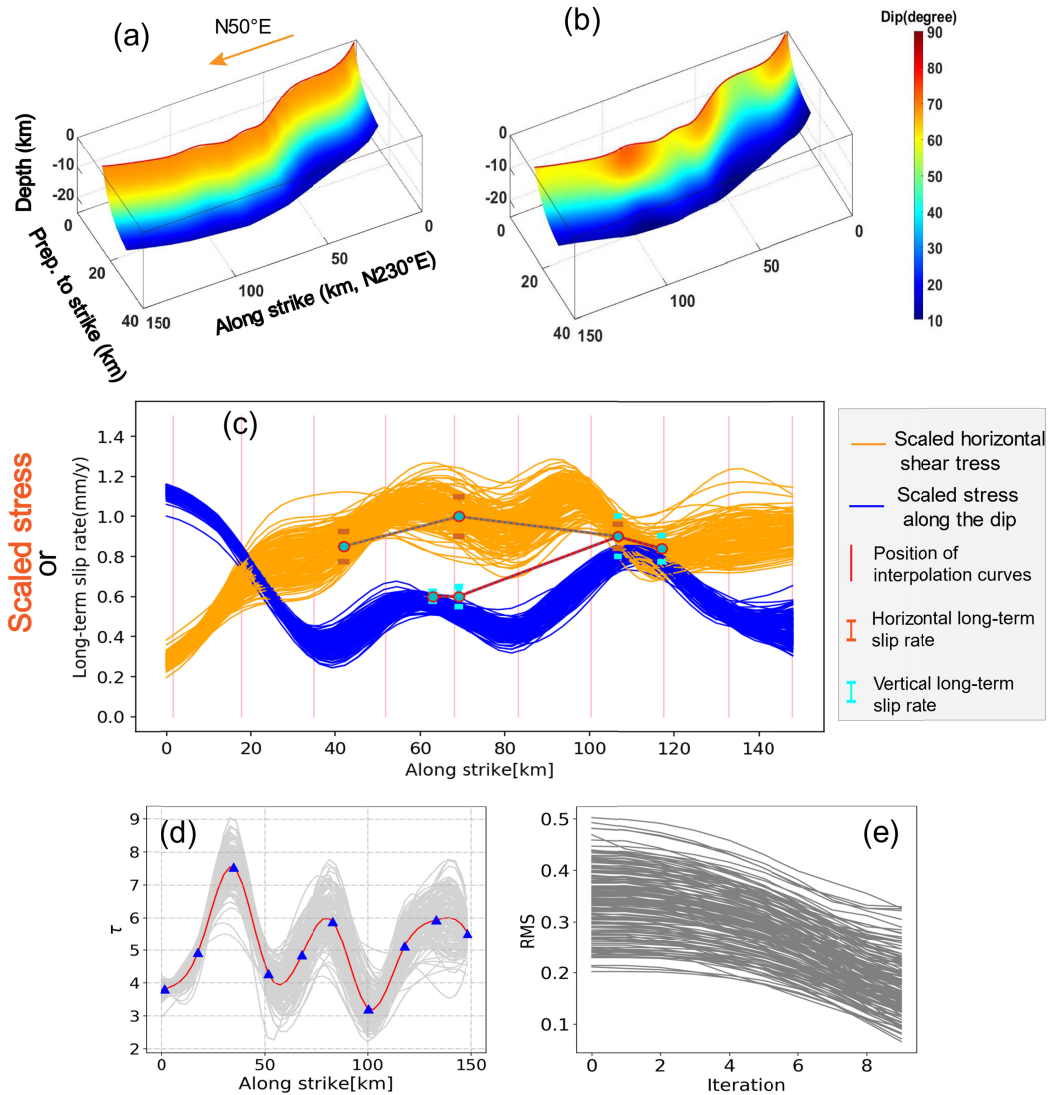
286
287
288
289

The average of 100 inversions is derived to obtain the final fault model (Figure 4b), where dip angles near the surface varied along the fault strike due to the constraint of observed long-term slip rates (Figure 4c). The final inversion results are distributed in a narrow strand (Figure 4d), and all objective functions steadily decrease versus the iterations (Figure 4e), which justifies our method.

290
291
292
293
294
295
296

While we believe that the present method of fault geometry inversion is a powerful and physically-based tool when we do not have sufficient subsurface data, this method should involve ambiguities due to the limitations of the available data and model constraints. Actual fault geometry can have a larger variation; Wan et al. (2017) inferred the fault dip for the Wenchuan earthquake using composite geodetic data and found that the BCF dips at 36° near the surface at its southwest end and is close to vertical (83°) at its northeast end at the surface. Differences in the dip angle can lead to differences in rupture scenarios and seismic risks for the BCF and WMF. A more detailed analysis will be conducted in our future study.

297
298



299
300
301
302
303
304
305
306
307
308

Figure 4 Estimation of fault geometry using 100 inversions. (a) Initial fault surface derived from the initial value of $\tau=5.0$, $h_0 = 18$. (b) Final fault surface derived from average τ of 100 inversions; The average of inverted fault depth $h_0 = 16.11$ is not shown here. (c) Observed long-term slip rates and scaled traction. The blue and orange lines present weighted average shear stress along the dip and strike, respectively. The length of the bar indicates the standard deviation of slip rate. The vertical thin pink lines indicate the position of interpolation curves. (d) Distribution of inverted parameters τ , the red line is the average of 100 inversions (gray lines), and blue triangles indicate the position of interpolation curves. (e) Objective functions versus iterations from 100 inversions.

309

310 **5. Dynamic rupture simulation**

311 **5.1. Method**

312 We computationally simulate spontaneous dynamic rupture propagation on the conjugate fault system of
 313 WMF and LXF. The dynamic rupture problems are numerically solved by the Fast Domain Partitioning
 314 Boundary Integral Equation Method (Ando, 2016; Ando et al., 2017; Ando et al., 2018), which increases
 315 the efficiency of the elastodynamic boundary equation method (BIEM) without degradation in accuracy.
 316 We consider a homogeneous elastic half space, with Lamé parameters $\lambda = \mu = 28 \text{ GPa}$, and mass density
 317 $\rho = 2776 \text{ kg/m}^3$ ($v_p = 5500 \text{ m/s}$, $v_s = 3175 \text{ m/s}$). These parameters are based on the first-order
 318 approximation of a three-dimensional velocity structure around the Longmen Shan fault obtained from
 319 seismic tomography (Pei et al., 2010; Wang et al., 2021). Note that the local variation of shallow seismic
 320 velocity structures or the site effect amplifying ground motion is not included in the present model. Rather,
 321 we focus on the source effect.

322 The boundary condition for the fault surface is considered where frictional strength is described by the
 323 linear slip weakening friction law

$$324 \quad T_s = \left(\mu_d + (\mu_s - \mu_d) \frac{S}{D_c} \right) T_n H(D_c - S) \quad (2)$$

325 Where D_c , μ_s and μ_d denote the characteristic slip, and the static and dynamic frictional coefficients,
 326 respectively. T_s and T_n denote the shear traction and normal stress. Based on the results of high-speed
 327 friction experiments (Yao et al., 2013), we set friction coefficients uniform on the entire fault with
 328 $\mu_s = 0.53$, $\mu_d = 0.12$. We choose $D_c = 0.8 \text{ m}$ because its upper bound is estimated in the range of
 329 1.0~2.0 m by Tang et al. (2021a), who applied the approach proposed by Mikumo et al. (2003) to estimate
 330 the upper bound of D_c of 2008 Wenchuan earthquake, constrained by the slip rates on the fault points
 331 from the kinematic inversion (Zhang et al., 2014) of complete near-field waveforms. The neighboring
 332 parameter space is also investigated and discussed in section 6, considering the uncertainties of these
 333 parameters. It is important to note that we first chose the relatively low μ_s , μ_d and D_c to allow the rupture
 334 to propagate to artificially assumed boundaries without being arrested, such that the worst earthquake
 335 scenarios can be explored.

336 In the simulation, ruptures are triggered by overstressing a small circle patch with a radius 3 km, where
 337 the initial stress is uniform and slightly above yield stress. Once a rupture is triggered, its subsequent
 338 development is controlled by the elastodynamic equation, frictional law, initial stress as well as fault
 339 geometry. While long-term slip rate and seismicity on the WMF indicate the potential to produce a large
 340 earthquake in the future, under our current state of knowledge, it is difficult to predict a probable
 341 hypocenter. Therefore, we considered five different nucleation locations, respectively located at the center,
 342 east and west ends of the WMF, and the north and south end of the LXF.

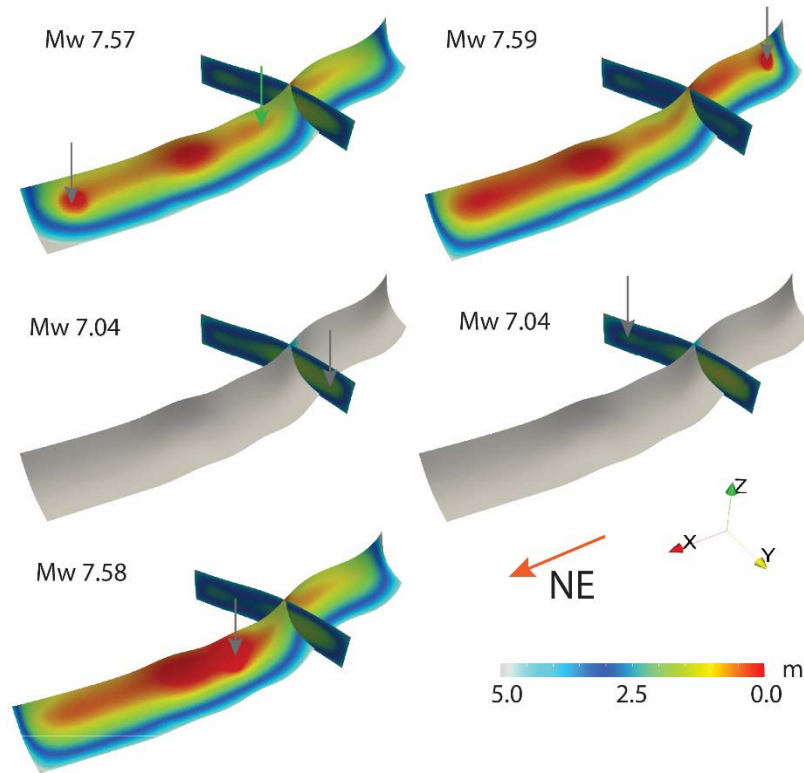
343 **5.2 Results**

344 **5.2.1 Coseismic slip**

345 Figure 5 shows the total slip distribution of the WMF and LXF, as well as the moment magnitude in each
 346 case. We find that the rupture tends to jump from the oblique-slip fault (WMF) to the strike-slip fault
 347 (LXF), but the reverse is more difficult. For instance, a dynamic rupture may start in the central, eastern
 348 or western parts of WMF, then cascade to the LXF, leading to three comparable-sized earthquakes with
 349 magnitude-7.56, 7.55 or 7.57. However, if it starts in the south or north of LXF, triggering a second

350 rupture on the WMF will be difficult (Figure 5, video S1-S2), leading to a smaller earthquake with a
351 moment magnitude 7.05 or 7.06.

352 The total slip on the LXF is smaller than that of the WMF. This might be surprising because the stress
353 drop on the LXF is significantly larger than that on the WMF (Figure S3). Noting that friction coefficients
354 on the two faults are exactly the same, so the prominent difference of the coseismic slips should be caused
355 by the faulting type and geometry. The WMF is a thrust fault with a larger extent in dip and strike than
356 LXF, which is a buried and smaller purely strike-slip fault. In the same stress condition, larger faults tend
357 to slip more due to the length-slip scaling. The free surface effect is further reduced for buried faults.
358 Besides, thrust faults have been proved by numerical simulations to have larger coseismic slips than
359 normal and strike-slip faults (Oglesby et al., 2002; Tang et al., 2021b), because the reflected waves from
360 the free surface amplify the motions of the reverse fault near the free surface. This result indicates reverse
361 faults may have greater destructive potential than strike-slip fault even though it is in a lower stress
362 condition.



363 Figure 5 Total slips and earthquake magnitudes from different nucleation points noted by grey arrows.
364 The green arrow denotes the point in Figure 13.
365
366

367 5.2.2 Peak Ground Displacement and Velocity

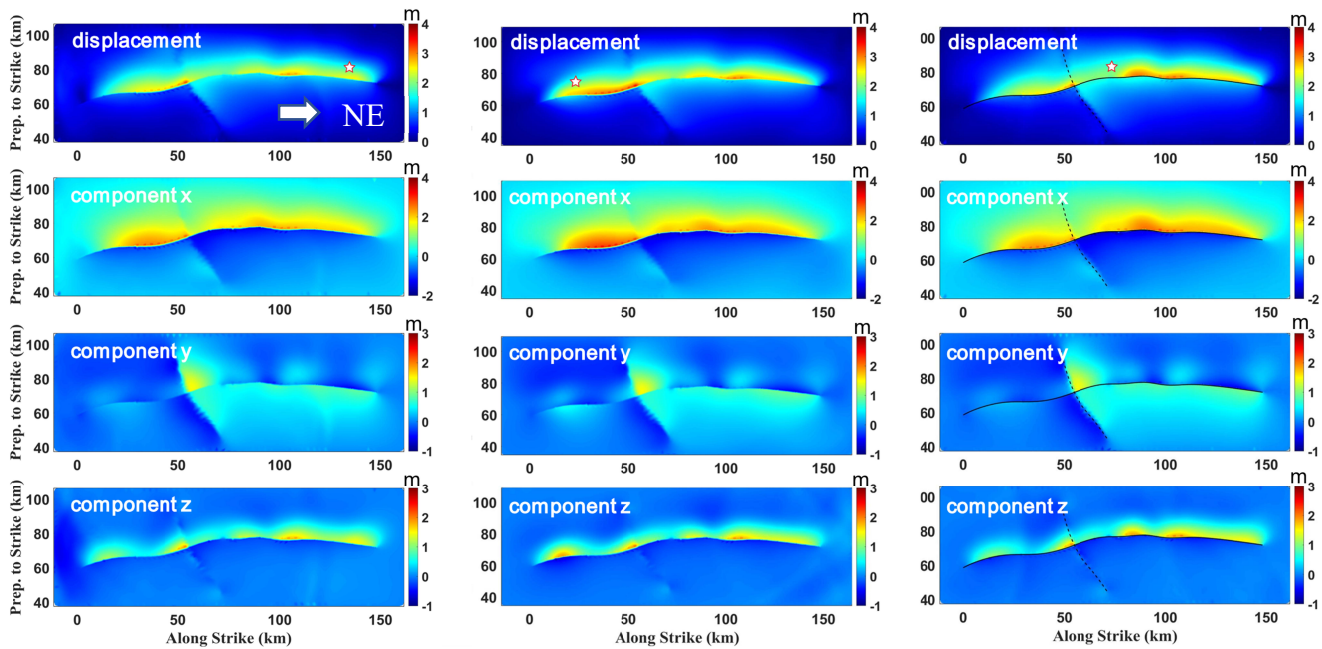
368 We evaluate the seismic risk potential, in a relative manner, by comparing derived surface displacements
369 (Figure 6) and peak ground velocities (PGV) (Figure 7). We find rupture directivity effects caused by
370 different nucleation positions lead to a prominent spatial difference in surface displacements and PGV.
371 The site where the rupture front propagates toward will suffer stronger ground motions than the site where

372 the rupture propagates away due to the cumulative effect of the seismic radiation called the forward
373 directivity (Somerville et al.,1997).

374
375 The ground motions of the hanging wall in the center and the eastern portion of WMF are significantly
376 enhanced if a rupture nucleates in the west and propagates to the eastern, compared to the cases when a
377 rupture starts in the west or center of the WMF (Figure 6 and Figure 7). These differences may be related
378 to the relationship between the hanging wall's horizontal movement and the rupture directivity, depending
379 on the different contributions of the horizontal slip component, because the components y and z are
380 almost the same for each case (Figure 6). We should care about a high seismic risk of the northeastern end
381 of the WMF in two cases (Figure 7 b, c) because the PGV is relatively high when a rupture nucleates at
382 the center or southwestern end of WMF, and the surface displacements are also high. From Figure 7 we
383 can further deduce that if the earthquake starts in most of the area on the WMF, the southwestern and
384 northeastern end of WMF may inevitably experience stronger ground motions.

385
386 Compared to the WMF, the PGV and surface displacements near the buried LXF are relatively low
387 because rupture does not break the surface (Figure 7 d, e). In addition, the rupture directivity shows
388 symmetry on strike-slip faults, and PGV shows a similar distribution when rupture starts from either north
389 or south of the LXF. However, for the WMF as an oblique-slip fault, the ground motion will be enhanced
390 if the rupture propagating direction is consistent with the movement direction of the hanging wall.

391



392

393

394 Figure 6 Three components and magnitude of surface slip, with eastern and western nucleation points.
395 The white Pentagrams denote the epicenter. The white arrow indicates the NE direction. See Figure 5 for
396 the definition of the x-y-z components.

397

398

399

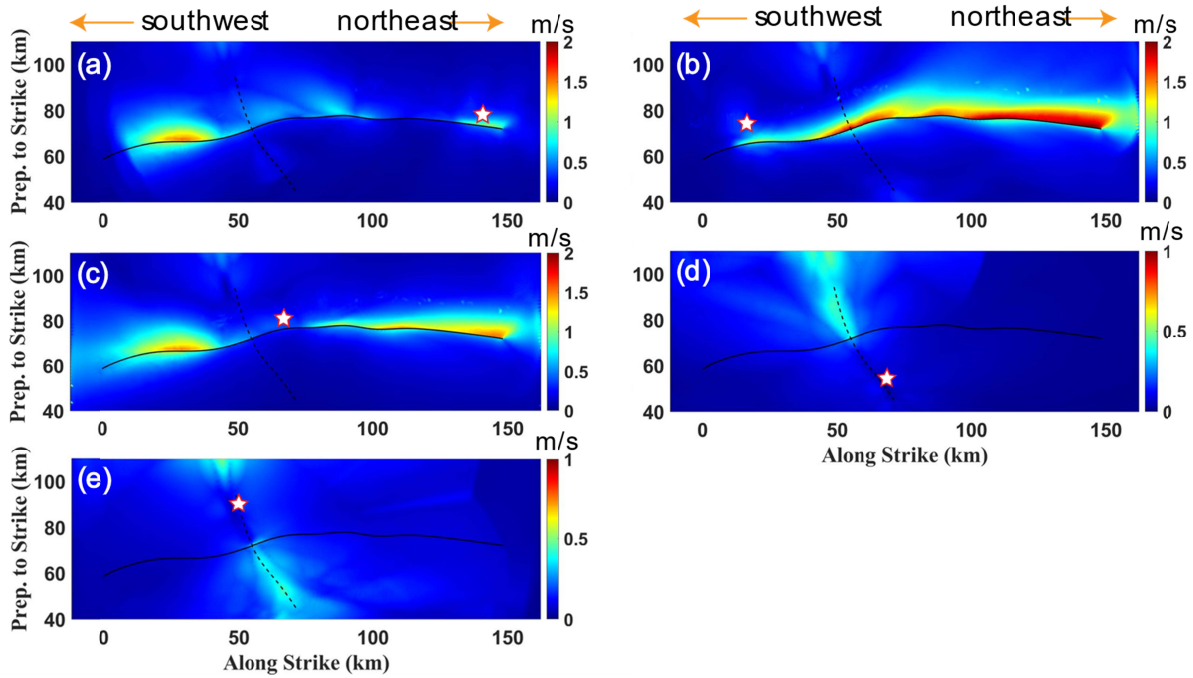


Figure 7 Magnitude of peak ground velocities from different nucleation points. The white pentagrams denote the epicenter.

6 Discussion

The worst-case scenarios have already been explored to evaluate the possible sizes of earthquakes and the distribution of strong ground motions. However, the results of dynamic rupture propagation are dependent on several key factors, including the initial stress, fault geometry, frictional parameters as well as hypocenters, which may lead to large uncertainty for different earthquake scenarios. For instance, different cases with a linear increase in stress from the surface down to some specified critical depth may result in a different distribution of ground motions as well as supershear transitions (Hu et al., 2021). To include this uncertainty, we change the specified depth but lower the maximum stress such that the same average stress drop can be held for the two cases (Figure 8). Without loss of generality, we model a total of 20 scenarios of dynamic rupture propagations (Table 1), to investigate the effects of neighboring parameter space, including μ_d (0.12~0.15) (Yao et al., 2013), D_c (0.8~1.2 m) (Tang et al., 2021a) and the critical depth of the stress increase.

Table 1
Models with a different set of friction and nucleation positions considered in this study.

Model	μ_d	D_c (m)	H of σ_v^* (km)	Depth of nucleation (km)	M_w	Arrest*	Dynamic triggering*	Total Seismic Moment (N m)
E1	0.12	0.8	5	6.5	7.57	No	Yes	2.893×10^{20}
W1	0.12	0.8	5	6.5	7.59	No	Yes	3.070×10^{20}
S1	0.12	0.8	5	6.5	7.04	No	No	4.686×10^{19}

N1	0.12	0.8	5	6.5	7.04	No	No	4.704×10^{19}
C1	0.12	0.8	5	6.5	7.58	No	No	3.048×10^{20}
E2	0.12	0.8	5	9.5	7.56	No	Yes	2.825×10^{20}
W2	0.12	0.8	5	9.5	7.59	No	Yes	3.060×10^{20}
E3	0.12	0.8	10	6.5	7.00	Yes	No	4.080×10^{19}
W3	0.12	0.8	10	6.5	7.56	No	Yes	2.823×10^{20}
N3	0.12	0.8	10	6.5	7.05	No	No	4.796×10^{19}
S3	0.12	0.8	10	6.5	7.05	No	No	4.774×10^{19}
C3	0.12	1.0	10	6.5	6.93	Yes	No	3.129×10^{19}
E4	0.15	0.8	5	6.5	6.92	Yes	No	3.118×10^{19}
W4	0.15	0.8	5	6.5	7.5	Yes	Yes	2.225×10^{20}
C4	0.15	0.8	5	6.5	7.42	Yes	Yes	1.703×10^{20}
W5	0.15	1.2	5	6.5	6.62	Yes	No	1.088×10^{19}
N5	0.15	1.2	5	6.5	7.00	No	No	4.109×10^{19}
S5	0.15	1.2	5	6.5	7.00	No	No	4.106×10^{19}
E5	0.15	1.2	5	6.5	6.65	Yes	No	1.207×10^{19}
C5	0.15	1.0	5	6.5	7.38	Yes	Yes	1.509×10^{20}

421
422
423
424
425
426
427

H of σ_v^* : the critical depth of the two different depth-dependent stress cases shown in Figure 9.
Arrest*: if Yes, the rupture will be arrested rather than reaching the assumed artificial barrier.
Dynamic triggering*: if Yes, the rupture on one fault will trigger the secondary rupture on the other fault.
The first letter of the model name represents the nucleation location, and E1~C1 have been elaborated in the result section.

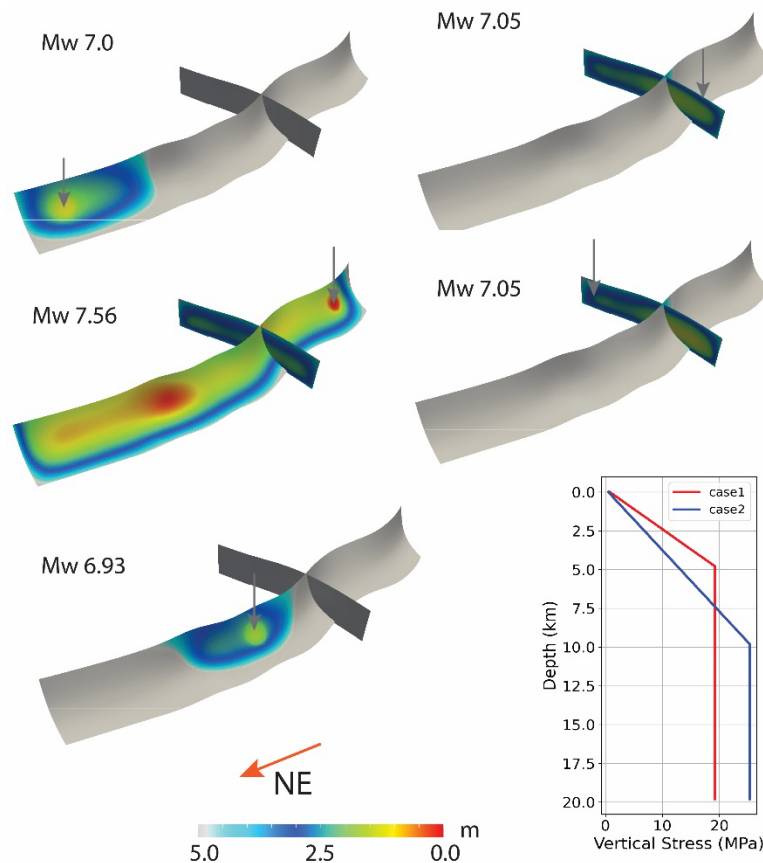
428

6.1 Effect of critical depth of stress

429
430
431
432
433
434
435
436
437
438
439
440
441
442
443

The average stress drops on the WMF and LXF are roughly obtained from observations from 2008 Wenchuan earthquake, but how is the distribution of stresses along the depth is poorly constrained. The magnitude of principal vertical stress depends on the overburden pressure (density and depth), which may also be compensated with the increased pore pressure (Hardebeck & Okada, 2018). Thus, we build two depth-dependent shear and normal stress regimes with the same average stress drop $\Delta\sigma_w = 2.9MPa$. The result of the first case has already been discussed in the result section, while the second case leads to the prominent different earthquake scenarios and distributions of the coseismic slip (Figure 8). For the second case with deeper critical depths, the ruptures starting in the east or center of the WMF propagate to 20 km beyond the nucleation area and arrest at the patch where the normal stress is stronger (Figure S3). In addition, the rupture from the west part propagates over the WMF and cascades to the LXF, but leads to lower magnitude (Table 1) and coseismic slips than that of W1 (Figure 5). However, contrary to the scenarios on the oblique fault (WMF), the coseismic slip and magnitudes on the sinistral fault (LXF) are slightly larger than that of case 1. These phenomena suggest that depth-dependent stress patterns may affect dip-slip faults more than strike-slip faults, and a larger stress gradient near the free surface of an oblique-slip fault is more likely to trigger stronger coseismic slip and higher seismic risk.

444
445



446
447
448
449
450
451

Figure 8 Simulations (model E3~C3 in Table 1) of the case 2 for depth-dependent vertical stress, the lower right sub-figure shows two different depth-dependent stress configurations with critical depth 5 km and 10 km.

452 6.2 Pattern of rupture in the WMF and LXF fault system

453

454 The earthquake scenarios from all simulations in Table 1 can be summarized as six patterns shown in
455 Figure 9a. The 20 cases tested do not cover the entire range of possibilities, and the assigned probabilities
456 remain arbitrary, such as uncertainty of geometry and initial stress are not fully considered. However, the
457 proposed scenarios in this study are fully understandable from the standpoint of the mechanics and,
458 therefore, appear likely. The spatial heterogeneity introduced in this study originates from fault geometry
459 and inverted regional stress, which principally controls the macroscopic patterns. For instance, cascading
460 ruptures tend to jump from oblique fault to strike-slip fault, but the reverse process is more difficult to
461 occur. The ruptures tend to be arrested on the WMF on serval parameter spaces while tend to easily run
462 through the entire LXF (Figure 9a). In addition, the rupture propagating eastward causes greater coseismic
463 displacements than the westward propagations.

464

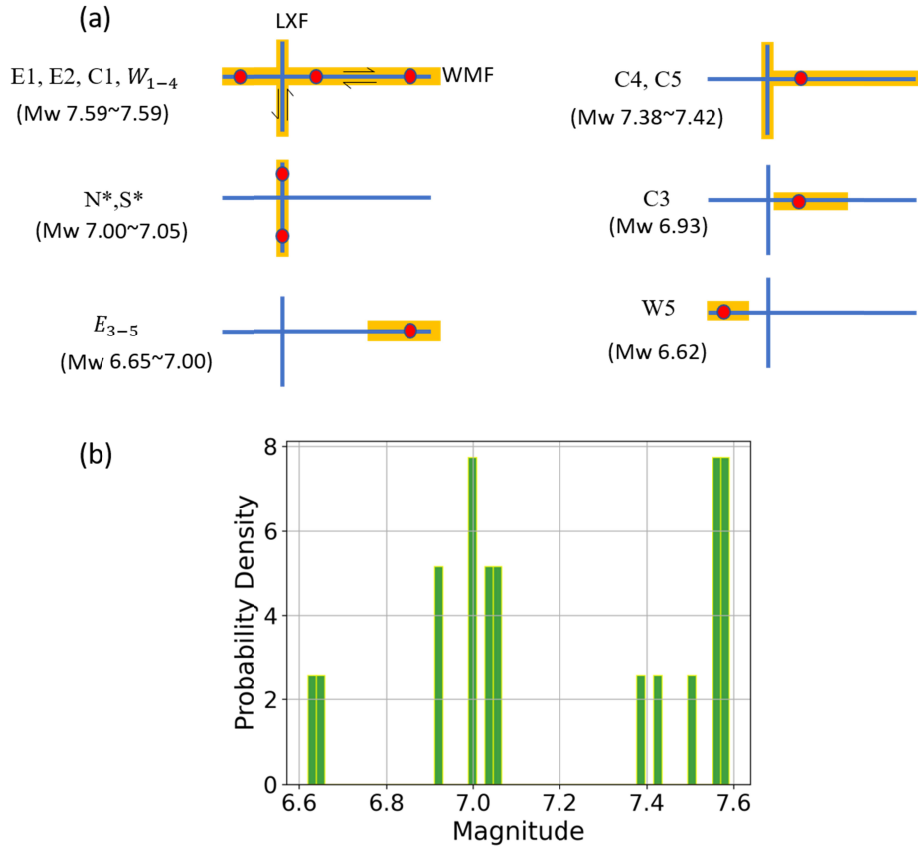
465 A statistical analysis of the moment magnitude, based on the deterministic simulation results, is presented
466 in Figure 9b. We find the earthquake scenarios fall into three groups: those of magnitudes are around 7.5,

467 7.0 or near 6.6. The first group gathers earthquakes that start on the WMF and could propagate all or most
468 parts of the two faults. The earthquakes with magnitudes around 7.0 usually come from the LXF, or local
469 ruptures on the WMF. The third group gathers earthquakes that start on the WMF but quickly stop near
470 the nucleation patch due to the unfavorable fault orientation given the friction parameters and on-fault
471 stress.

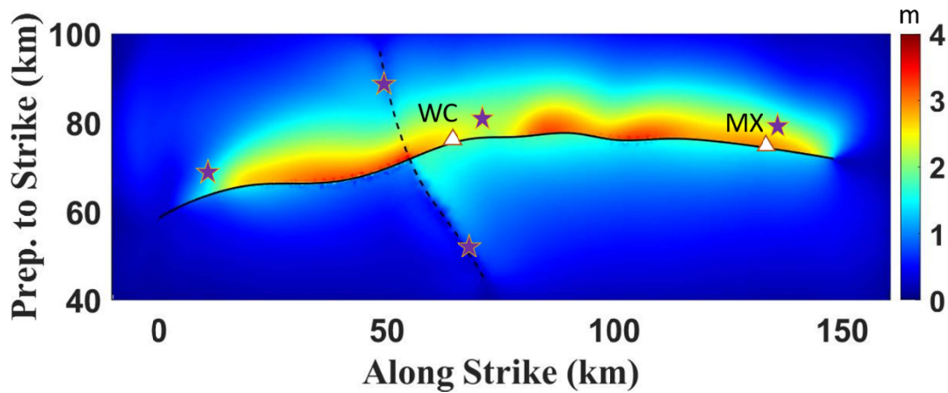
472
473 Incorporating all earthquake scenarios to further assess the possible seismic risk in the future, we calculate
474 the maximum surface displacements shown in Figure 10. Static surface deformation plays a crucial role in
475 near-source earthquake hazard analysis. In 2008 Wenchuan Earthquake, the maximum surface
476 displacements are distributed in the two patches underneath Yingxiu and Beichuan towns, leading to the
477 two areas suffering the most intensive shock (Hao et al., 2009; Shen et al., 2009; Tang et al., 2021a).
478 From Figure 10, we find that the two prominent peaks are distributed in the areas of 40 km and 100 km
479 along-strike distance. The Wenchuan town is near the edge of the moderate slip, while the Maoxian town
480 are in the range of the larger slip. Besides, the PGV distributions from the worst scenarios indicate PGV is
481 relatively high when a rupture nucleates at the center or eastern end of WMF. Consequently, Waoxian can
482 suffer a higher seismic risk than Wenchuan in the viewpoint of the source processes .

483
484 We also find the value of $\mu_d = 0.12\sim 0.15$ from all modes are slightly lower than those used in
485 Wenchuan earthquake simulations ($\mu_d = 0.18$) (Zhang et al., 2019; Tang et al., 2021a). If the same
486 friction parameters are used in this study, ruptures will be hard to break in the designed nucleation zone.
487 This is because the steeper dip angle near the surface of the WMF (Figure 4) tends to increase the normal
488 stress, enhancing the fault clamping effect and making it more difficult to slip. Thus, if our model of the
489 WMF with the steeper dip angle is correct, the WMF may cause the lower seismic risk than the BCF with
490 a lower dip for a long-term geological time.

491
492
493
494



495
496
497
498
499
Figure 9 Slip patterns from all models using simple schematic diagrams (a) and histogram of the magnitudes (Mw) obtained in the 20 simulations (b). Yellow highlighting indicates the path of propagating rupture, and solid red circles denote the nucleation sites.



500
501
502
503
504
Figure 10 The map for maximum surface displacements from 20 simulations. The white triangles present the two main cities (Wenchuan and Maoxian) and red stars denote the epicenters.

505 6.3 Explanation for rupture Patterns

506 We have completed the simulation of the worst earthquake scenarios (model E1~C1), and predicted
507 possible high seismic risk areas. It is noted that there are two interesting scientific issues worthy of further

508 discussion. First, why do cascading ruptures tend to jump from oblique fault to strike-slip fault, but the
509 reverse process is more difficult? Second, why does the rupture propagating eastward cause greater
510 coseismic displacements than the westward propagation? Although we have mentioned that the rupture
511 directivity can explain the second question, here we hope to further explore the deeper reasons from the
512 perspective of mechanics.
513

514 To answer the first question, we calculate the shear stress changes $\Delta\tau$ and normal stress change $\Delta\sigma$
515 (positive in compression), as well as the Coulomb failure stress change (ΔCFS) on the two faults, under
516 the state when a rupture is approaching the fault intersection (Figure 11). ΔCFS is calculated from
517 $\Delta CFS = \Delta\tau - \mu_s \Delta\sigma$ (Harris,1998), measuring whether the fault tends to be slip (positive) or stable
518 (negative) (Freed, 2005; Parsons et al.,2008; Liu et al.,2018). We found that the rupture nucleating at the
519 east or west end of the WMF approaches the fault intersection can induce obvious positive ΔCFS on the
520 LXF. The main contribution of the increase in ΔCFS comes from $\Delta\tau$ rather than $\Delta\sigma$, although the normal
521 stress change affects a larger area on the LXF. On the other hand, the rupture nucleating at the north or
522 south end of the LXF approaches the fault intersection can induce obvious negative ΔCFS on the WMF.
523 The ΔCFS in the most area near the intersection of the WMF is negative, although there are small-scale
524 positive ΔCFS locally. The ΔCFS is decreased because the effect of shear stress reduction is lower than
525 that of the normal stress increase, or the effect of shear stress reduction is larger than that of normal stress
526 reduction.
527

528 It is noted that the fault activity depends on its prestress state besides ΔCFS . However, it is more difficult
529 to observationally determine the absolute prestress level or when in its seismic cycle than the principal
530 stress orientation and the stress ratio. We should keep in mind that the prediction can be more complicated
531 if we consider further stress heterogeneity than those in our modeling. With such a limitation, compared
532 to the WMF, the LXF possibly has higher initial shear stress (Figure S3). This result means that the LXF
533 will be closer to failure than the WMF. As a consequence, together with the evolution of ΔCFS for the
534 four cases, it is reasonable to expect the cascading ruptures jumping from the oblique fault to the strike-
535 slip fault rather than the reverse propagation.
536
537
538

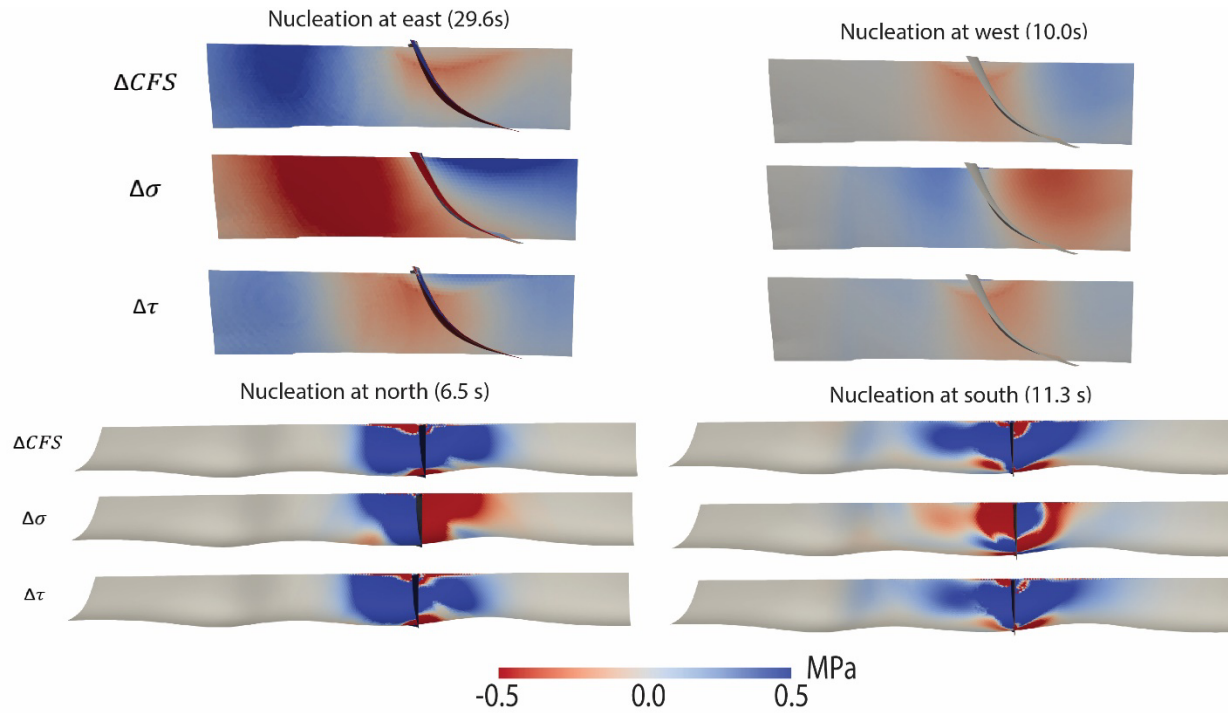


Figure 11 Stress change near the fault intersection when rupture is approaching. Coulumb failure stress $\Delta CFS(t) = \Delta\tau(t) - \mu_d \Delta\sigma(t)$, where $\Delta\tau$ is shear stress change, $\Delta\sigma$ normal stress change

With regard to the second question, why does the rupture propagating eastward cause greater coseismic slips than the westward propagation. We emphasize that all the conditions in two cases are the same except for the different nucleation position or rupture propagating directivity. The increase of coseismic slips in figure 5b than 5a are distributed almost over the entire fault rather than a local area, which means the stress evolution at a certain point (such as the point shown in Figure 5) on the fault may help reveal the physical mechanism of this phenomenon (Figure 12). The variation of shear stress in two cases are similar in the two cases and the dynamic stress drops are the same, while the normal stress suddenly increases when the rupture propagates from east to west (Figure 12a). The seismic waves generated by rupture superimpose on the edge of rupture front, couple with the hanging wall moving in opposite direction (oblique and dextral slip), forming a local compression. This transient increase of normal stress has suppressed slip rate to reach a large peak value (Figure 12c), resulting in a lower coseismic slip than that of reverse propagating directivity. Our result is consistent with the study of Tang et al (2021b).

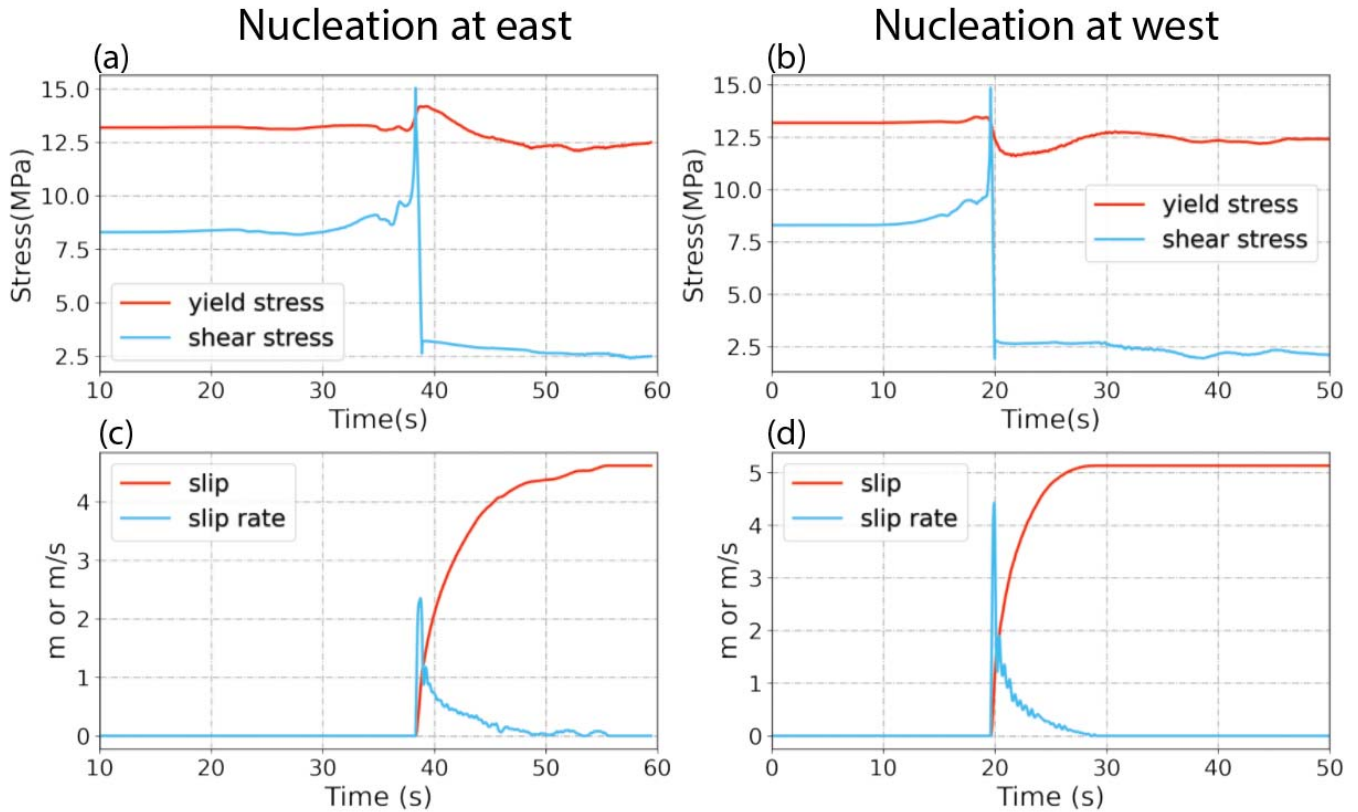


Figure 12 Evolution of stress and slip for the cases with different nucleation positions. The location of fault point is indicated in Figure 5.

558
559
560
561
562
563
564

565 **7 Conclusion**

566 In this study, we demonstrate an effective technical process, including inversion techniques of the
567 regional tectonic stress and fault geometry, to simulate a dynamic process of active faults, which is
568 helpful in predicting a future earthquake scenario.

569 We have developed a new algorithm based on the stress state and the Wallace-Bott hypothesis for
570 inversion of fault geometry, and we have obtained non-planar fault surfaces with heterogenous dip angles.
571 In the absence of other geophysical or geological data to constrain fault geometry, this is an effective
572 scheme to obtain relatively accurate faults, with only a small number of long-term slip rate data being
573 used.

574 Combining deterministic simulations of earthquake dynamics makes it possible to quantify probable
575 rupture scenarios for future earthquakes in the target area, the fault system of the Wenchuan-Maoxian
576 Fault and Lixian Fault. This process is to clarify the mechanical causality of the dynamic system.
577 Numerical simulation results forecast the possible size of the earthquakes occurring on the WMF and
578 LXF in the future while the timing is out of focus. The potential high seismic risk areas are found to be
579
580

581 largely dependent on where the earthquake nucleates. In addition, we have two general conclusions with
582 regard to the system of a reverse oblique fault with a conjugate strike-slip fault. Due to the positive
583 Coulomb Failure Stress change near the fault intersection, the rupture starting on the reverse oblique-slip
584 tends to jump to the strike-slip fault, but the reverse process is difficult because negative Coulomb Failure
585 Stress change dominates near the intersection. Besides, the ground motion will be enhanced if the rupture
586 propagating direction is consistent with the movement direction of the hanging wall because a local
587 compression forms in the counterpart case, suppressing the coseismic slip.
588

589 **Acknowledgement**

592 Acknowledgement for the data support from China Earthquake Networks Center, National
593 Earthquake Data Center (<https://data.earthquake.cn/>). Videos in this paper can be download from
594 <https://zenodo.org/record/7077841#.YyGRFnZBxD8>. This work is supported in part by MEXT, Japan,
595 under its Earthquake and Volcano Hazards Observation and Research Program, and Basic Scientific
596 Research Program from Yangtze Delta Region Institute (U032200109), as well as China Scholarship
597 Council. Oakforest-PACS in University of Tokyo was used for the numerical simulations under the "Joint
598 Usage/Research Center for Interdisciplinary Large-scale Information Infrastructures" and "High
599 Performance Computing Infrastructure" in Japan (Project ID: jh210023-NAH). The authors thank Junjie
600 Ren, So Ozawa and Tawei Chang for providing helpful suggestions.
601

602 **Reference**

- 603
- 604
- 605 Ando, R. (2016). Fast domain partitioning method for dynamic boundary integral equations applicable to
606 non-planar faults dipping in 3-D elastic half-space. *Geophysical Journal International*, 207(2), 833–
607 847. <https://doi.org/10.1093/gji/ggw299>
- 608 Ando, R., Imanishi, K., Panayotopoulos, Y., & Kobayashi, T. (2017). Dynamic rupture propagation on
609 geometrically complex fault with along-strike variation of fault maturity: Insights from the 2014
610 northern Nagano earthquake. *Earth, Planets and Space*, 69(1). <https://doi.org/10.1186/s40623-017-0715-2>
- 611
- 612 Ando, R., & Kaneko, Y. (2018). Dynamic rupture simulation reproduces spontaneous multifault rupture
613 and arrest during the 2016 Mw 7.9 Kaikoura earthquake. *Geophysical Research Letters*, 45(23), 12-
614 875.
- 615 Anderson, E.M. (1951) The dynamics of faulting and dike formation with application to Britain. Oliver
616 and Boyd, 2nd Edition, Edinburgh, 133147. Bott, M.H.P., 1959. The mechanisms of oblique slip
617 faulting, *Geol. Mag.*, 96, 109–117.
- 618 Cai, C., Yu, C., Tao, K., Hu, X., Tian, Y., Zhang, H., ... & Ning, J. (2011). Spatial distribution and focal
619 mechanism solutions of the Wenchuan earthquake series: Results and implications. *Earthquake*
620 *Science*, 24(1), 115-125.

- 621 Chen, Z. H., Burchfiel, B. C., Liu, Y., King, R. W., Royden, L. H., Tang, W., ... & Zhang, X. (2000).
622 Global Positioning System measurements from eastern Tibet and their implications for India/Eurasia
623 intercontinental deformation. *Journal of Geophysical Research: Solid Earth*, 105(B7), 16215-16227.
- 624 DENG Wen-Ze, CHEN Jiu-Hui, GUO Biao, LIU Qi-Yuan, LI Shun-Cheng, LI Yu, YIN Xin-Zhong, QI
625 Shao-Hua. Fine velocity structure of the Longmenshan fault zone by double-difference
626 tomography[J]. *Chinese Journal of Geophysics*, 2014, 57(4): 1101-1110. doi: 10.6038/cjg20140408
- 627 Douilly, R., Aochi, H., Calais, E., & Freed, A. M. (2015). Three-dimensional dynamic rupture simulations
628 across interacting faults: The Mw7. 0, 2010, Haiti earthquake. *Journal of Geophysical Research:*
629 *Solid Earth*, 120(2), 1108-1128.
- 630 DING, Y. Y., & LI, Z. K. (2009). The discovery of the geophysical field boundary along Wudu-Wenxian-
631 Lixian line and its significance. *Geology in China*, 6.
- 632 Feng, G., Jónsson, S., & Klinger, Y. (2017). Which fault segments ruptured in the 2008 Wenchuan
633 earthquake and which did not? New evidence from near-fault 3D surface displacements derived from
634 SAR image offsets. *Bulletin of the Seismological Society of America*, 107(3), 1185-1200.
- 635 Farquharson, C. G., & Oldenburg, D. W. (2004). A comparison of automatic techniques for estimating the
636 regularization parameter in non-linear inverse problems. *Geophysical Journal International*, 156(3),
637 411-425.
- 638 Hardebeck, J. L., & Michael, A. J. (2006). Damped regional-scale stress inversions: Methodology and
639 examples for southern California and the Coalinga aftershock sequence. *Journal of Geophysical*
640 *Research: Solid Earth*, 111(B11).
- 641 Hubbard, J., Shaw, J. H., & Klinger, Y. (2010). Structural Setting of the 2008 Mw 7.9 Wenchuan, China,
642 EarthquakeStructural Setting of the 2008 Mw 7.9 Wenchuan, China, Earthquake. *Bulletin of the*
643 *Seismological Society of America*, 100(5B), 2713-2735.
- 644 Hu, F., Oglesby, D. D., & Chen, X. (2021). The effect of depth-dependent stress in controlling free-
645 surface-induced supershear rupture on strike-slip faults. *Journal of Geophysical Research: Solid*
646 *Earth*, e2020JB021459.
- 647 Jia, D., Li, Y., Lin, A., Wang, M., Chen, W., Wu, X., ... & Luo, L. (2010). Structural model of 2008 Mw
648 7.9 Wenchuan earthquake in the rejuvenated Longmen Shan thrust belt,
649 China. *Tectonophysics*, 491(1-4), 174-184.
- 650 Kanamori, H., & Anderson, D. L. (1975). Theoretical basis of some empirical relations in
651 seismology. *Bulletin of the seismological society of America*, 65(5), 1073-1095.
- 652 Li, Y., Jia, D., Shaw, J. H., Hubbard, J., Lin, A., Wang, M., ... & Wu, L. (2010). Structural interpretation
653 of the coseismic faults of the Wenchuan earthquake: Three-dimensional modeling of the Longmen
654 Shan fold-and-thrust belt. *Journal of Geophysical Research: Solid Earth*, 115(B4).
- 655 Li, X., Hergert, T., Henk, A., Wang, D., & Zeng, Z. (2019). Subsurface structure and spatial segmentation
656 of the Longmen Shan fault zone at the eastern margin of Tibetan Plateau: Evidence from focal
657 mechanism solutions and stress field inversion. *Tectonophysics*, 757, 10-23.
- 658 Liu-Zeng, J., Zhang, Z., Wen, L., Tapponnier, P., Sun, J., Xing, X., ... & Ji, C. (2009). Coseismic ruptures
659 of the 12 May 2008, Ms 8.0 Wenchuan earthquake, Sichuan: East-west crustal shortening on oblique,
660 parallel thrusts along the eastern edge of Tibet. *Earth and Planetary Science Letters*, 286(3-4), 355-
661 370.
- 662 Lozos, J. C., & Harris, R. A. (2020). Dynamic rupture simulations of the M6. 4 and M7. 1 July 2019
663 Ridgecrest, California, earthquakes. *Geophysical Research Letters*, 47(7), e2019GL086020.
- 664 Lu, R., He, D., John, S., Wu, J. E., Liu, B., & Chen, Y. (2014). Structural model of the central Longmen
665 Shan thrusts using seismic reflection profiles: Implications for the sediments and deformations since
666 the Mesozoic. *Tectonophysics*, 630, 43-53.

667 Ma, B., Su, G., Hou, Z., & Shu, S. (2005). Late quaternary slip rate in the central part of the Longmen
668 Shan fault zone from terrace deformation along the Minjiang River. *Seismology and Geology*, 27(2),
669 234–242.

670 Matsumoto, S., Yamashita, Y., Nakamoto, M., Miyazaki, M., Sakai, S., Iio, Y., ... & Asano, Y. (2018).
671 Prestate of stress and fault behavior during the 2016 Kumamoto earthquake (M7. 3). *Geophysical*
672 *Research Letters*, 45(2), 637-645.

673 Michael, A. J. (1987). Stress rotation during the Coalinga aftershock sequence. *Journal of Geophysical*
674 *Research: Solid Earth*, 92(B8), 7963-7979.

675 Michael, A. J. (1984). Determination of stress from slip data: faults and folds. *Journal of Geophysical*
676 *Research: Solid Earth*, 89(B13), 11517-11526.

677 Mikumo, T., Olsen, K. B., Fukuyama, E., & Yagi, Y. (2003). Stress-breakdown time and slip-weakening
678 distance inferred from slip-velocity functions on earthquake faults. *Bulletin of the Seismological*
679 *Society of America*, 93(1), 264-282.

680 Marquardt, D. W. (1963). An algorithm for least-squares estimation of nonlinear parameters. *Journal of*
681 *the society for Industrial and Applied Mathematics*, 11(2), 431-441.

682 Madden, T. R., and Mackie, R. L., 1989, Three-dimensional magnetotelluric modeling and inversion,
683 *Proc. IEEE*, 77, 318–333.

684 Mackie, R. L., and Madden, T. R., 1993, Three-dimensional magnetotelluric inversion using conjugate
685 gradients: *Geophys. J. Internat.*, 115, 215–229.

686 McKinley, S., & Levine, M. (1998). Cubic spline interpolation. *College of the Redwoods*, 45(1), 1049-
687 1060.

688 Xu, X., Wen, X., Yu, G., Chen, G., Klinger, Y., Hubbard, J., & Shaw, J. (2009a). Coseismic reverse-and
689 oblique-slip surface faulting generated by the 2008 Mw 7.9 Wenchuan earthquake,
690 China. *Geology*, 37(6), 515-518.

691 Oglesby, D. D., Archuleta, R. J., & Nielsen, S. B. (2000). The three-dimensional dynamics of dipping
692 faults. *Bulletin of the Seismological Society of America*, 90(3), 616-628.

693 Ran, Y. K., Chen, W. S., Xu, X. W., Chen, L. C., Wang, H., Yang, C. C., & Dong, S. P. (2013).
694 Paleoseismic events and recurrence interval along the Beichuan–Yingxiu fault of Longmenshan fault
695 zone, Yingxiu, Sichuan, China. *Tectonophysics*, 584, 81-90.

696 Ran, Y., Chen, L., Chen, J., Wang, H., Chen, G., Yin, J., ... & Xu, X. (2010). Paleoseismic evidence and
697 repeat time of large earthquakes at three sites along the Longmenshan fault
698 zone. *Tectonophysics*, 491(1-4), 141-153.

699 Reches, Z. E. (1987). Determination of the tectonic stress tensor from slip along faults that obey the
700 Coulomb yield condition. *Tectonics*, 6(6), 849-861.

701 Rice, J. R. 1992. Fault stress states, pore pressure distributions, and the weakness of the San Andreas fault.
702 In *International geophysics* (Vol. 51, pp. 475-503). Academic Press

703 Rice J R. 1993. Spatio-temporal complexity of slip on a fault. *Journal of Geophysical Research*. 98
704 (B6),9885-9907.

705 Rodi, W., & Mackie, R. L. (2001). Nonlinear conjugate gradients algorithm for 2-D magnetotelluric
706 inversion. *Geophysics*, 66(1), 174-187.

707 Shen, Z.-K., Sun, J., Zhang, P., Wan, Y., Wang, M., Bürgmann, R., et al. (2009). Slip maxima at fault
708 junctions and rupturing of barriers during the 2008 Wenchuan earthquake. *Nature Geoscience*, 10,
709 718–724.

710 Shearer, P. M., Prieto, G. A., & Hauksson, E. (2006). Comprehensive analysis of earthquake source
711 spectra in southern California. *Journal of Geophysical Research: Solid Earth*, 111(B6).

- 712 Soh, I., Chang, C., Lee, J., Hong, T. K., & Park, E. S. (2018). Tectonic stress orientations and magnitudes,
713 and friction of faults, deduced from earthquake focal mechanism inversions over the Korean
714 Peninsula. *Geophysical Journal International*, 213(2), 1360-1373.
- 715 Somerville, P. G., Smith, N. F., Graves, R. W., & Abrahamson, N. A. (1997). Modification of empirical
716 strong ground motion attenuation relations to include the amplitude and duration effects of rupture
717 directivity. *Seismological research letters*, 68(1), 199-222.
- 718 Tang, R., Zhu, S., & Gan, L. (2021a). Dynamic Rupture Simulations of the 2008 7.9 Wenchuan
719 Earthquake: Implication for Heterogeneous Initial Stress and Complex Multifault Geometry. *Journal*
720 *of Geophysical Research: Solid Earth*, 126(12), e2021JB022457.
- 721 Tang, R., Yuan, J., & Gan, L. (2021b). Free-Surface-Induced Supershear Transition in 3-D Simulations of
722 Spontaneous Dynamic Rupture on Oblique Faults. *Geophysical Research Letters*, 48(3),
723 e2020GL091621.
- 724 Tian, T., Zhang, J., Liu, T., Jiang, W., & Zhao, Y. (2017). Morphology, tectonic significance, and
725 relationship to the Wenchuan earthquake of the Xiaoyudong Fault in Western China based on gravity
726 and magnetic data. *Journal of Asian Earth Sciences*, 138, 672-684.
- 727 Trugman, D. T., & Shearer, P. M. (2017). Application of an improved spectral decomposition method to
728 examine earthquake source scaling in Southern California. *Journal of Geophysical Research: Solid*
729 *Earth*, 122(4), 2890-2910.
- 730 Ulrich, T., Gabriel, A. A., Ampuero, J. P., & Xu, W. (2019). Dynamic viability of the 2016 Mw 7.8
731 Kaikōura earthquake cascade on weak crustal faults. *Nature communications*, 10(1), 1-16.
- 732 Vavryčuk, V. (2014). Iterative joint inversion for stress and fault orientations from focal
733 mechanisms. *Geophysical Journal International*, 199(1), 69-77.
- 734 Wu, J., Yao, D., Meng, X., Peng, Z., Su, J., & Long, F. (2017). Spatial-temporal evolutions of early
735 aftershocks following the 2013 Mw 6.6 Lushan earthquake in Sichuan, China. *Journal of*
736 *Geophysical Research: Solid Earth*, 122, 2873–2889. <https://doi.org/10.1002/2016JB013706>
- 737 Wan, Y., Shen, Z. K., Bürgmann, R., Sun, J., & Wang, M. (2016). Fault geometry and slip distribution of
738 the 2008 Mw 7.9 Wenchuan, China earthquake, inferred from GPS and InSAR
739 measurements. *Geophysical Journal International*, ggw421.
- 740 Wang, Z., Wang, J., & Yang, X. (2021). The role of fluids in the 2008 Ms8. 0 Wenchuan
741 earthquake. *Journal of Geophysical Research: Solid Earth*, 126, e2020JB019959.
- 742 Wallace, R.E., 1951. Geometry of shearing stress and relation to faulting, *J. Geol.*, 59, 118–130.
- 743 WU, J. P., HUANG, Y., ZHANG, T. Z., MING, Y. H., & FANG, L. H. (2009). Aftershock distribution of
744 the MS8. 0 Wenchuan earthquake and 3-DP-wave velocity structure in and around source
745 region. *Chinese Journal of Geophysics*, 52(1), 102-111.
- 746 Xie Xinheng, Jiang Wali, Feng Xiyang .2011.Discussi on on appearance of surface fractures along the
747 rear-range of Longmen shan mountain during 2008 Ms8.0 Wenchuan earthquake .*Acta Seismologica*
748 *Sinica*, 33(1):62- 81
- 749 Xu, X., Wen, X., Yu, G., Chen, G., Klinger, Y., Hubbard, J., & Shaw, J. (2009). Coseismic reverse-and
750 oblique-slip surface faulting generated by the 2008 Mw 7.9 Wenchuan earthquake,
751 China. *Geology*, 37(6), 515-518.
- 752 Xu, X., Zhang, Z., Hu, F., & Chen, X. (2019). Dynamic Rupture Simulations of the 1920 Ms 8.5 Haiyuan
753 Earthquake in ChinaDynamic Rupture Simulations of the 1920 Ms 8.5 Haiyuan Earthquake in
754 China. *Bulletin of the Seismological Society of America*, 109(5), 2009-2020.
- 755 Yang, N., & Zhang, Y. Q. (2010). Tission-track dating for activity of the Longmenshan fault zone and
756 uplifting of the western Sichuan Plateau. *Journal of Geomechanics (in Chinese)*, 16(4), 359-371.

757 Yao, D., Walter, J. I., Meng, X., Hobbs, T. E., Peng, Z., Newman, A. V., et al. (2017). Detailed
758 spatiotemporal evolution of microseismicity and repeating earthquakes following the 2012 Mw 7.6
759 Nicoya earthquake. *Journal of Geophysical Research: Solid Earth*, 122, 524–542.
760 <https://doi.org/10.1002/2016JB013632>

761 Yin, X. Z., Chen, J. H., Peng, Z., Meng, X., Liu, Q. Y., Guo, B., & Li, S. C. (2018). Evolution and
762 distribution of the early aftershocks following the 2008 Mw 7.9 Wenchuan earthquake in Sichuan,
763 China. *Journal of Geophysical Research: Solid Earth*, 123(9), 7775-7790.

764 Yi, G., Long, F., & Zhang, Z. (2012). Spatial and temporal variation of focal mechanisms for aftershocks
765 of the 2008 MS8. 0 Wenchuan earthquake. *Chinese Journal of Geophysics*, 55(4), 1213-1227.

766 Zhao, B., Shi, Y., & Gao, Y. (2011). Relocation of aftershocks of the Wenchuan M S 8.0 earthquake and
767 its implication to seismotectonics. *Earthquake Science*, 24(1), 107-113.

768 Zhang, Y., Feng, W., Xu, L., Zhou, C., & Chen, Y. (2009). Spatio-temporal rupture process of the 2008
769 great Wenchuan earthquake. *Science in China Series D-Earth Sciences*, 52(2), 145–154.

770 Zhang, Y., Wang, R., Zschau, J., Chen, Y. T., Parolai, S., & Dahm, T. (2014). Automatic imaging of
771 earthquake rupture processes by iterative deconvolution and stacking of high-rate GPS and strong
772 motion seismograms. *Journal of Geophysical Research: Solid Earth*, 119(7), 5633-5650.

773 Zhdanov, M. S. (2002). *Geophysical inverse theory and regularization problems* (Vol. 36). Elsevier.
774
775
776
777